JOURNAL OF SOLID STATE CHEMISTRY 40, 52–58 (1981)

A New Monoclinic Phase in the Fe_2O_3–TiO_2 System. II. The Defect Structure

V. KRAŠEVEC,* A. PRODAN, M. BAKKER,† M. DROFENIK, L. GOLIČ, D. HANŽEL, AND D. KOLAR

Jožef Stefan Institute, Edvard Kardelj University, Jamova 39, 61000 Ljubljana, Yugoslavia

Received March 19, 1981; in revised form June 11, 1981

Defects in monoclinic Fe_2TiO_5 were studied by electron microscopy and diffraction. The monoclinic structure found, which is isostructural with V_3O_5, can be derived in a simple way from a hexagonal close-packed structure and can be considered as a member of the family of crystallographic shear structures, derived from rutile. Two different slips corresponding to two hexagonal basal ones, were found to cause stacking faults, antiphase boundaries, and two different crystallographic shear planes.

Introduction

In part I of this paper (*1*) the preparation, structure, and some magnetic properties of monoclinic Fe_2TiO_5 were described. The structure is a polytype of pseudobrookite (*2*) and is metastable at room temperature. A rather high R factor in the X-ray analysis, as well as the line broadening of Mössbauer spectra, is indicative of a certain disorder in the arrangement of TiO_6 and FeO_6 octahedra in the structure. In this part a more detailed description of the structure in relation to other oxide structures will be given, in order to understand better the electron microscopic observations, which will be presented later.

Description of the Structures

The monoclinic structure Fe_2TiO_5 is isostructural with V_3O_5 (*3*), Ti_3O_5 (*4*), and $FeCrTiO_5$ (*5*, *6*). It is projected onto the $(020)_m$ plane in Fig. 1 and onto the $(20\bar{1})_m$

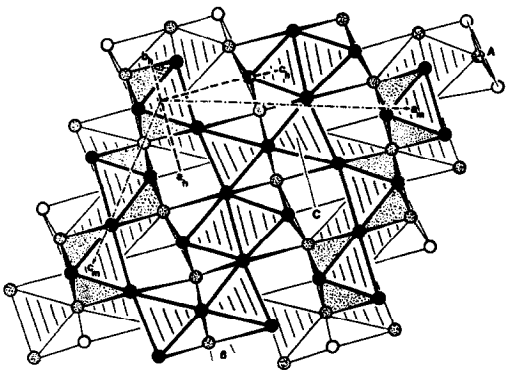

FIG. 1. The structure of monoclinic Fe_2TiO_5 with the unit cell vectors for both the monoclinic and the related hcp structure. Vectors A and C correspond to the possible slip directions. The deformation of the hexagonal basal planes is indicated by the angle β.

* Author to whom correspondence should be addressed.

† On leave from Gorlaeus Laboratories, University of Leiden, P.O. Box 9502, 2300 RA Leiden, The Netherlands.

0022-4596/81/130052-07$02.00/0

plane in Fig. 2a. These projections emphasize two structural relations. The first shows that the anions form a distorted hexagonal close-packed (hcp) sublattice. Considering an ideal hcp, it is possible to relate the monoclinic and hexagonal unit cells with the following transformation matrices:

planes

	a_m	b_m	c_m
a_h	$\frac{1}{5}$	0	$\frac{2}{5}$
b_h	$-\frac{1}{10}$	$-\frac{1}{2}$	$-\frac{1}{5}$
c_h	$\frac{2}{5}$	0	$-\frac{1}{5}$

	a_h	b_h	c_h
a_m	1	0	2
b_m	−1	−2	0
c_m	2	0	−1

(1a)

vectors

	a_m	b_m	c_m
a_h	1	−1	2
b_h	0	−2	0
c_h	2	0	−1

	a_h	b_h	c_h
a_m	$\frac{1}{5}$	$-\frac{1}{10}$	$\frac{2}{5}$
b_m	0	$-\frac{1}{2}$	0
c_m	$\frac{2}{5}$	$-\frac{1}{5}$	$-\frac{1}{5}$

(1b)[1]

[1] The threefold hexagonal indices should be further transformed into the fourfold notation.

The cations partly fill the octahedral interstices in the hcp array. In each column, three out of five face-shared octahedra are filled, which gives the following ideal sequence for each column: –Fe–Fe–□–Ti–□–Fe–Fe–□–Ti–□–, etc. This indicates that the structure is related to that of rutile on one hand and to that of corundum on the other (*7*):

–Ti–□–Ti–□–Ti–□–	TiO_2,
–Fe–Fe–□–Fe–Fe–□–Fe–Fe–	Al_2O_3.

The projections of Fig. 2 clarify this relation. The structure can be derived by means of a crystallographic shear (*CS*) operation from the rutile structure (*8*), where the relationship between the hexagonal and the rutile structures is given by the following transformation matrices:

planes

	a_h	b_h	c_h
a_r	0	0	1
b_r	2	1	0
c_r	0	1	0

	a_r	b_r	c_r
a_h	0	$\frac{1}{2}$	$-\frac{1}{2}$
b_h	0	0	1
c_h	1	0	0

(2a)

vectors

	a_h	b_h	c_h
a_r	0	0	1
b_r	$\frac{1}{2}$	0	0
c_r	$-\frac{1}{2}$	1	0

	a_r	b_r	c_r
a_h	0	2	0
b_h	0	1	1
c_h	1	0	0

(2b)

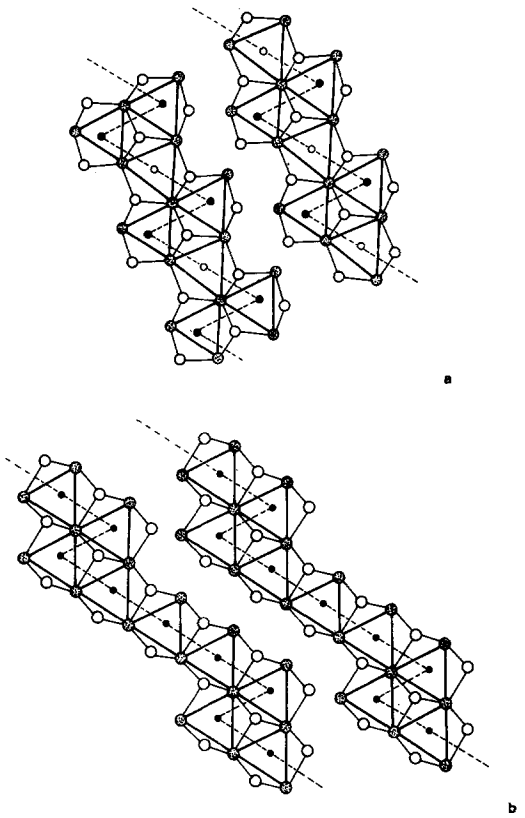

FIG. 2. (a) The structure of monoclinic Fe_2TiO_5 projected onto the $(20\bar{1})_m$ plane. Dotted lines indicate the rutile *CS* slabs 3,3,3,3. (b) The structure of Ti_5O_9 projected onto the $(\bar{1}11)_r$ plane. The dotted lines indicate the rutile *CS* slabs 5,5,5,5.

Therefore this structure fits into the scheme of a homologous series of Ti_nO_{2n-1} structures, obtained from rutile by regularly repeated *CS* operations. The displacement vector is $\frac{1}{2}[0\bar{1}1]_r$ and the *CS* planes are of the type $(hkl)_r = p(121)_r + q(011)_r$, where the first is the *CS* and the second the antiphase boundary (*APB*) component (*8–10*). It has a slab sequence 3,3,3,3, and can be compared with the structure of Ti_5O_9 with a slab sequence 5,5,5,5, which is projected onto the $(\bar{1}11)_r$ plane in Fig. 2b (*11*).

Experimental

Specimens for transmission electron microscopy were prepared either by argon-ion erosion of thin crystals or by grinding the crystals into fine pieces, which were then dispersed onto holey carbon films. Some of the crystals were already transparent for 100-keV electrons and these were observed without additional thinning. A Philips EM-301 electron microscope equipped with a goniometer stage was used.

Results and Discussion

In general the electron diffraction patterns taken from monoclinic Fe_2TiO_5 were compatible with the X-ray analysis. However, some characteristic features were always observed in the diffraction patterns of certain zones. Figure 3a shows the charac-

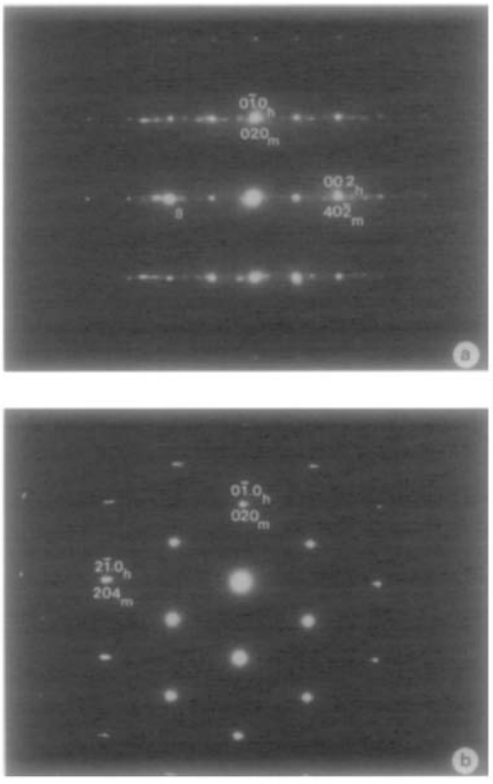

FIG. 3. (a) The diffraction pattern of the $[\bar{1}0\bar{2}]_m$ zone. Note the split streaking at one-third of the distance of the $[20\bar{1}]^*_m$ spacing. (b) The diffraction pattern of the $[\bar{2}01]_m$ zone. Note the hexagonal symmetry.

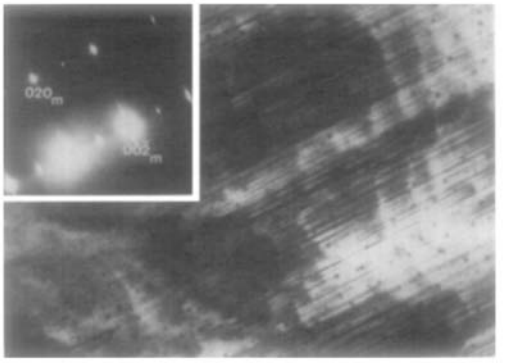

FIG. 4. Irregularly spaced *APB*s parallel to the $(020)_m$ planes. The electron beam is along the $[100]_m$ zone axis. Magnification 40,000×.

teristic split streaking at one-third of the distance of the $[20\bar{1}]^*_m \equiv [00.1]^*_h$ spacing in the diffraction pattern of the $[\bar{1}0\bar{2}]_m \equiv [\bar{2}1.0]_h$ zone. The streaking is due to stacking faults perpendicular to the hexagonal $[00.1]_h$ direction. This means that locally fcc instead of hcp stacking is formed by three different slip systems, $(20\bar{1})_m\frac{1}{3}[010]_m$, $(20\bar{1})_m\frac{1}{30}[356]_m$, and $(20\bar{1})_m\frac{1}{30}[\bar{3}56]_m$, corresponding to three equivalent $(00.1)_h\frac{1}{3}\langle 10.0\rangle_h$ hexagonal ones. These stacking faults are formed because the monoclinic structure is unstable with respect to the room temperature structure of pseudobrookite. The origin of the split streaking is the slight deformation of the hcp anion sublattice, where most of the octahedra planes form an angle β with respect to the $(00.2)_h$ planes. This angle is indicated in Fig. 1 as well as in the diffraction pattern of Fig. 3a. Another prominent zone, the $[\bar{2}01]_m \equiv [00.1]_h$ one, is shown in Fig. 3b. The hexagonal symmetry of the diffraction pattern is evident.

Besides these stacking faults several other types of planar defects were observed. Analyzing the oxygen–oxygen vectors in the hexagonal structure one finds six possible equivalent slip vectors: $\pm\frac{1}{3}[2\bar{1}.0]_h$, $\pm\frac{1}{3}[\bar{1}2.0]_h$, and $\pm\frac{1}{3}[\bar{1}\bar{1}.0]_h$. Using the matrix (1b) these can be transformed into the monoclinic vectors $\pm\frac{1}{5}[102]_m$, $\pm\frac{1}{10}[152]_m$ and $\pm\frac{1}{10}[\bar{1}52]_m$, where only the first two can take place because of the cation vacancies present. When the slip vector is parallel to the plane it operates on, the result is an *APB*. However, when the slip is in a plane which is nonparallel to the slip vector the result is a *CS* operation (slip plus shear). The last operation can account for nonstoichiometry (*8, 10*).

Figure 4 represents the electron micrograph and the corresponding diffraction pattern, with the beam parallel to the $[100]_m$ zone axis, of a region containing parallel planar defects. The strong streaking along $[020]^*_m$ is due to irregularly spaced faults parallel to the $(020)_m$ planes, as evident from the micrograph. These defects can be produced by $(020)_m\frac{1}{5}[102]_m = (0\bar{1}.0)_h\frac{1}{3}[2\ \bar{1}.0]_h$ slip operation and can consequently be characterized as *APB*s (*13*). These were usually observed in thermally untreated specimens. Using the transformation matrices (2) it is evident that these *APB*s correspond to the rutile $(\bar{0}\bar{1}\bar{1})_r\frac{1}{2}[01\bar{1}]_r$ ones, which are the *APB* components in the *CS* structures derived from rutile (*10*).

In Fig. 5 the same $[100]_m$ zone is shown, but the streaking is now along $[002]^*_m$. The *CS* operation producing these defects is

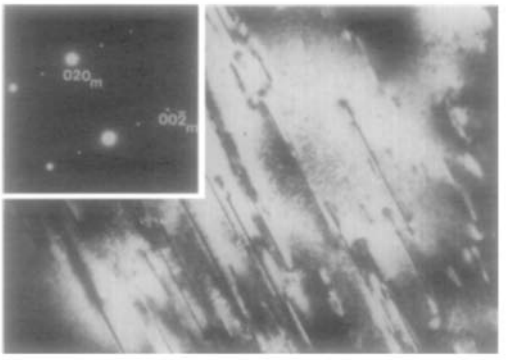

FIG. 5. DF image taken with the $(00\bar{2})_m$ reflection, showing *CS* planes parallel to the $(002)_m$ planes. The electron beam is along the $[100]_m$ zone axis. Magnification 40,000×.

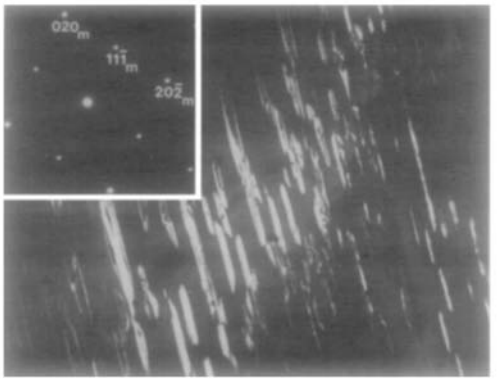

FIG. 6. DF image taken with the $(11\bar{1})_m$ reflection, of the *CS* planes, shown edge-on in Fig. 5. The electron beam is along the $[\bar{1}0\bar{1}]_m$ zone axis. Magnification 20,500×.

$(002)_m\frac{1}{3}[102]_m \equiv (4\bar{2}.\bar{2})_h\frac{1}{3}[2\bar{1}.0]_h$. They always appeared immediately after slight pulse beam heating. Further, they originate at the surface and grow into the sample, as can be seen from Fig. 6, where the nucleating knife-shaped shear planes are shown with the sample tilted out of the above mentioned zone. Only one of the surface edges is straight, if these *CS* planes are small. By growing, the defect plane reaches the second surface, while the growth is continued in the two perpendicular directions. Simultaneously, the lateral growth of the sheared region is accomplished by generating successive *CS* planes. With the use of the transformation matrices (2) these *CS* defects were found to correspond to the rutile $(\bar{2}6\bar{2})_r\frac{1}{2}[01\bar{1}]_r$ ones. These can be further decomposed into two components: $(\bar{2}4\bar{2})_r\frac{1}{2}[01\bar{1}]_r + 5(020)_r\frac{1}{2}[01\bar{1}]_r$. The first one is the well known *CS* component of the defects found in the rutile $[\bar{1}11]_r$ zone (*10*), while the second one was found to be stable in the rutile structure above 1720K, forming slabs of the NiAs structure (*12*).

Another type of defect is U-shaped and appears after prolonged pulse beam heating (Fig. 7). During heating they propagate parallel to the length direction, and can reach the edge of the foil. Additional defects often grow concentrically inside the already existing ones, as described by Van Landuyt and Amelinckx (*14*) for hairpin-shaped *CS* planes. The planes of the long components form an angle of about ±28° with the $(020)_m$ planes as shown by tilting experiments. These defects can be produced by $(110)_m\frac{1}{3}[102]_m \equiv (1\bar{3}.2)_h\frac{1}{3}[2\bar{1}.0]_h$ and $(1\bar{1}0)_m\frac{1}{3}[102]_m \equiv (12.2)_h\frac{1}{3}[2\bar{1}.0]_h$ *CS* operations, respectively, and they were seen edge-on by tilting the crystal around $[002]_m^*$ until either $(110)_m$ or $(1\bar{1}0)_m$ planes were parallel to the electron beam. In Fig. 8 one

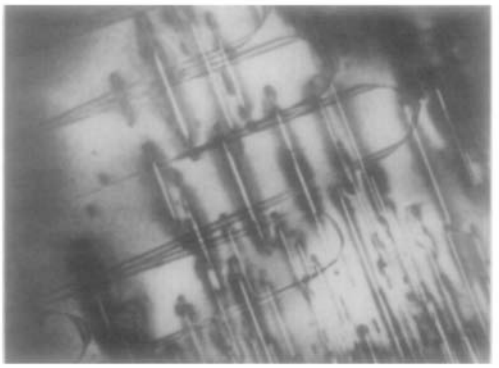

FIG. 7. U-shaped *CS* planes with the long components parallel to the $(110)_m$ and $(1\bar{1}0)_m$ planes, respectively. The corresponding diffraction pattern is the same as in Fig. 4. Magnification 20,500×.

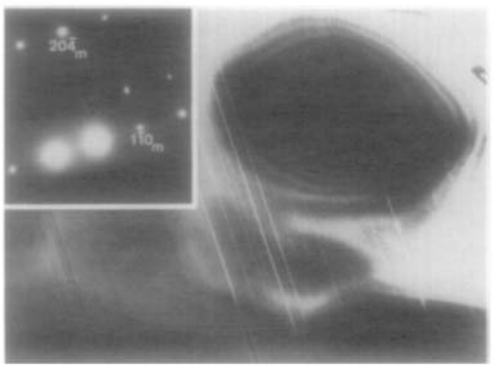

FIG. 8. *CS* planes parallel to the $(1\bar{1}0)_m$ planes. The beam is along the $[221]_m$ zone axis. Magnification 20,500×. Additional reflections from the $[\bar{1}00]_m$ zone are also visible.

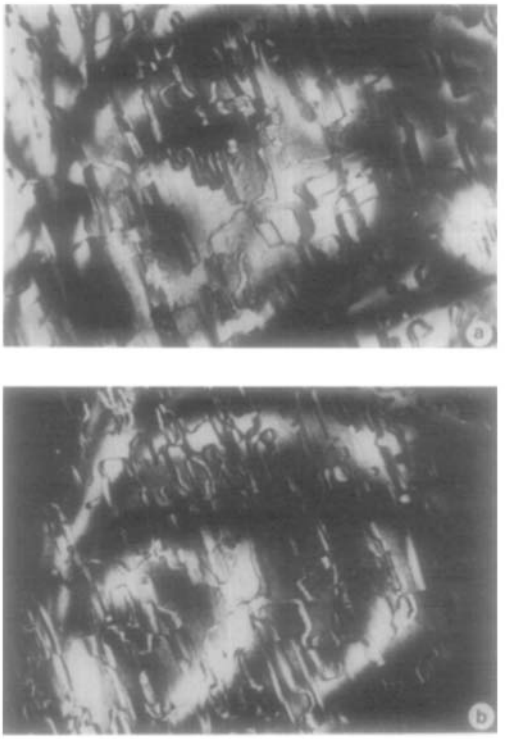

FIG. 9. (a) BF image of *CS* planes as observed in very thin regions. The beam is along the $[\bar{1}0\bar{1}]_m$ zone axis. (b) DF image of the same region as under Fig. 9a, using the $(11\bar{1})_m$ reflection. The corresponding diffraction pattern is the same as in Fig. 6. Magnification 40,000×.

set of these planes is seen edge-on in the $[221]_m$ zone. From the final thickness of most of these defects it follows that the *CS* planes are grouped. The two components of this type of defect correspond to the $(2\bar{1}\bar{3})_r\frac{1}{2}[01\bar{1}]_r$ and $(242)_r\frac{1}{2}[01\bar{1}]_r$ rutile ones, respectively. The first can again be decomposed into $(242)_r\frac{1}{2}[01\bar{1}]_r - 5(011)_r\frac{1}{2}[01\bar{1}]_r$, with a pure *CS* and a pure *APB* component, while the second fits a *CS* component only (*10*).

In very thin foils the appearance of all these defects is slightly different, as seen from Figs. 9a and b, which are the BF and DF taken by the $(11\bar{1})_m$ reflection, respectively. The corresponding diffraction pattern is, however, the same as in Fig. 6. It is evident that the fringes of the longer components are symmetrical in BF and asymmetrical in DF, which are characteristics of the α fringes. These longer components are parallel to the $(002)_m$ planes. Some of these defects are of finite thickness and change of contrast takes place where individual planes along the defects are terminated by dislocations. The different form of the same defects in very thin regions is supposed to be due to an easier stress relief in such regions.

The defects formed by *CS* are often of a finite thickness, as shown schematically in Fig. 10. It is evident that different mechanisms are responsible for the growth of the two kinds of defects. While in the knife-shaped defects additional *CS* planes are generated at one surface of the sample and grow into the depth, the growth mechanism of the U-shaped ones involves the movement of the front of additional *CS* planes in the $[002]_m$ direction. It is not clear as yet

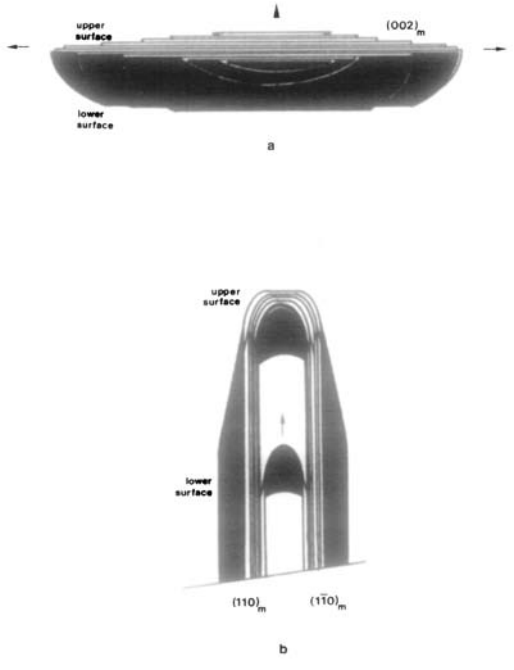

FIG. 10. Schematic representation of knife-shaped (a) and U-shaped (b) defects formed by *CS* planes. The directions of growth are indicated by arrows.

why apparently more energy is needed to generate the U-shaped defects.

Conclusions

It was shown that the structure of monoclinic Fe_2TiO_5 can be derived from an hcp structure, where the anion sublattice remains a slightly distorted hcp one, while the cation sublattice is obtained by removing cations in an ordered way from such a lattice.

Different defect formation mechanisms were found to generate stacking faults in the $(20\bar{1})_m$ planes, *APB*s in the $(020)_m$ planes, and two different *CS* planes in $(002)_m$ and $(110)_m/(1\bar{1}0)_m$ planes, respectively. Very often the *CS* planes grow together, forming bulky defects of characteristic shapes.

The monoclinic Fe_2TiO_5 structure can also be related to the rutile structure, derived from the same hcp parent structure. The defects observed fit well with some known defects in the rutile structure.

Acknowledgments

The authors acknowledge with appreciation the assistance during the experimental work of Mrs. Z. Škraba and the financial support of the Boris Kidrič Foundation.

References

1. M. DROFENIK, L. GOLIČ, D. HANŽEL, V. KRAŠEVEC, A. PRODAN, M. BAKKER, AND D. KOLAR, *J. Solid State Chem.* **40**, 47 (1981).
2. R. W. G. WYCKOFF, "Crystal Structures," Vol. 3. Wiley, New York (1964).
3. S. ÅSBRINK, S. FRIBERG, A. MAGNÉLI, G. ANDERSSON, *Acta Chem. Scand.* **13**, 603 (1959).
4. G. ÅSBRINK, S. ÅSBRINK, A. MAGNÉLI, H. OKINAKA, K. KOSUGE, AND S. KACHI, *Acta Chem. Scand.* **25**, 3889 (1971).
5. I. E. GREY AND A. F. REID, *J. Solid State Chem.* **4**, 186 (1972).
6. I. E. GREY, A. F. REID, AND J. G. ALLPRESS, *J. Solid State Chem.* **8**, 86 (1973).
7. H. D. MEGAW, "Crystal Structures—A Working Approach," Saunders, Philadelphia (1973).
8. L. A. BURSILL AND B. G. HYDE, "Progress in Solid State Chemistry" (H. Reiss and J. O. McCaldin, Eds.), Vol. 7, p. 177. Pergamon Press, Oxford (1972).
9. L. A. BURSILL, *J. Solid State Chem.* **10**, 72 (1974).
10. B. G. HYDE, A. N. BAGSHAW, S. ANDERSSON, AND M. O'KEEFE, *Annu. Rev. Mater. Sci.* **4**, 43 (1974).
11. S. ANDERSSON, *Acta Chem. Scand.* **14**, 1161 (1960).
12. L. A. BURSILL, I. E. GREY, AND D. J. LLOYD, *J. Solid State Chem.* **16**, 331 (1976).
13. S. AMELINCKX AND R. J. D. TILLEY, *J. Solid State Chem.* **2**, 472 (1970).
14. J. VAN LANDUYT AND S. AMELINCKX, *J. Solid State Chem.* **6**, 222 (1973).